RhoA regulates membrane order and tension to control excitability of nociceptor neurons

Soheila Sabouri[1,#], Lucas J. Handlin[1,#], Clémence Gieré[2], Nicolas L.A. Dumaire[2], Natalie L. Macchi[1], Donald W. Hilgemann[3], Aubin Moutal[2], and Gucan Dai[1,*]

[1]Edward A. Doisy Department of Biochemistry & Molecular Biology, Saint Louis University School of Medicine, 1100 South Grand Blvd., St. Louis, MO, USA

[2]Department of Pharmacology and Physiology, Saint Louis University School of Medicine, St. Louis, MO, USA

[3]Department of Physiology, University of Texas Southwestern Medical Center, Dallas, TX, USA

[#]Equal Contributions

[*]Correspondence: Gucan Dai (gucan.dai@health.slu.edu)

Abstract

Compartmentalization of the plasma membrane into phase-separated domains has emerged as a fundamental principle in regulating membrane transport and excitability[1-3]. However, it remains unclear how neuropathic stress initiates lipid remodeling of membrane domains. Here we show a previously unrecognized role for the monomeric GTPase RhoA in driving the coalescence of ordered membrane domains (OMDs)[4], coupling cytoskeletal dynamics to membrane fluidity and order. Using FLIM-based Förster resonance energy transfer, we quantified nanoscale changes in OMD size in living cells[3]. Pharmacological modulation of RhoA activity altered OMD size in both human cell lines and nociceptor dorsal root ganglion (DRG) neurons. Optogenetic activation of RhoA using an improved light-inducible dimerization system triggered rapid OMD coalescence[5-7]. Moreover, RhoA-mediated remodeling of OMDs required an intact cytoskeletal network and was driven by heightened membrane lateral tension, a response that was also dependent on protein palmitoylation. Functionally, RhoA inhibition increased action potential firing and potentiated pacemaker HCN channel activity in nociceptive DRG neurons. Conversely, in a spared nerve injury model—where DRG neurons display small OMDs, reduced membrane tension, and hyperexcitability—RhoA activation enlarged OMDs, suppressed HCN channel activity, and dampened neuronal excitability. Together, these findings suggest RhoA-driven OMD remodeling as a key adaptive mechanism that counteracts the hyperexcitability associated with neuropathic pain. They further highlight reduced membrane tension as a biophysical signature of neuropathic stress and suggest that targeting the RhoA pathway may offer a therapeutic strategy for chronic pain.

Main

Cell membranes are laterally heterogeneous, composed of lipid domains that vary in composition and size and act as platforms for localized cell signaling[2,8]. One major type of domain, termed liquid ordered (L_o) or ordered membrane domain (OMD), is characterized by its high levels of cholesterol and sphingolipids. OMDs vary in size and tend to be thicker than liquid disordered (L_d) or disordered membrane domains[9,10]. This type of membrane phase separation is characterized by the dynamic ability of OMDs to coalesce into larger or separate into smaller domains[9]. Importantly, lipid domains have been associated with many biological processes, including Alzheimer's disease[11,12], viral infections[13], immune signaling[8,14], and neuropathic pain[3,15]. Given their critical role in normal cellular function, it is essential to identify key regulators of OMD dynamics.

RhoA, a small monomeric GTPase belonging to the Ras superfamily, has numerous well-known cellular functions, including regulation of actin cytoskeleton (actin stress fibers and assembly of focal adhesions), cell migration, cell shape, and endocytosis[16-19]. Guanine nucleotide exchange factors (GEFs) are responsible for the exchange of GDP for GTP and therefore activate RhoA[17,20]. Inactive, GDP-bound RhoA is predominantly cytosolic, whereas active, GTP-bound RhoA associates with the plasma membrane to engage downstream effectors. In contrast, RhoB mostly associates with endosome membranes, whereas RhoC, structurally more similar to RhoA, localizes to the plasma membrane and tends to be dysregulated during various types of cancer[21]. Importantly, RhoA activity is elevated markedly following peripheral nerve injury, important for nerve regeneration[22]. Cytokines, particularly those involved in neuroinflammation after nerve damage (e.g., TNF-α and IL-1β), stimulate GEFs to promote RhoA signaling in neurons[23-25]. In addition, following nerve injury, myelin-derived proteins such as myelin-associated glycoprotein (MAG) and Nogo-A, as well as signaling lipid sphingosine-1-phosphate (S1P) and lysophosphatidic acid (LPA) also activate RhoA in peripheral neurons[24,26-28]. In summary, RhoA, a membrane-associated small GTPase, is a central regulator of the cytoskeleton in sensory neurons and a mediator of the signaling cascade that regulates nerve regeneration. A less understood aspect of its function, however, is its influence on the biophysical properties of the lipid bilayer and the resulting implications for neuronal excitability.

Emerging evidence indicates that activation of small G proteins drives an OMD-dependent, clathrin/dynamin-independent type of endocytosis known as OMD endocytosis (OMDE) or massive endocytosis (MEND)[29-33]. Upon stimulation by various types of cell stress, the plasma membrane reorganizes to coalesce OMDs which subsequently serve as sites for initiating endocytosis[30,32,34]. Overall, OMDE is enhanced by supplementation with pyruvate, moderate concentration of palmitate/albumin

complexes, and calcium transients, but is inhibited by fatty acid deprivation, treatment with 2-bromopalmitate/albumin complexes, blockade of the mitochondrial permeability transition pore (PTP), or inhibition of palmitoyl acyltransferases (e.g., DHHC enzymes)[29-32,34]. Given the established links between OMDE, cytoskeletal remodeling, and RhoA activation[32], we aimed to define the effects of RhoA activation on OMD properties.

Here we use fluorescence lifetime imaging microscopy (FLIM) combined with Förster resonance energy transfer (FRET) to investigate how RhoA activity influences OMD size. We provide evidence supporting that RhoA activation promoted the coalescence of OMDs through cytoskeleton remodeling and modulating membrane lateral tension. Furthermore, RhoA inhibition alters pacemaker HCN channel activity and action potential firing in sensory neurons, likely via its effects on OMDs. Inhibition of the HCN activity by RhoA activation and the resulting dampening of membrane hyperexcitability may have evolved as an adaptation to chronic pain. These findings reveal a mechanistic link between small GTPases, cytoskeleton, lipid domains, membrane tension and excitability.

Rho activation and inhibition modulate OMD size assessed by FLIM-FRET

Cholera toxin subunit B (CTxB) conjugated FRET pairs were used as probes to determine relative changes in OMD size[3]. These probes are pentamers derived from *Vibrio cholerae* and have a high affinity for GM1 gangliosides, a type of sphingolipid found at high levels in OMDs[35,36]. Whereas conventional fluorescence microscopy has limitations due to the diffraction limit of light (~250 nm), FRET-based fluorescence overcomes this limitation and can visualize lipid domains with nanometer-level sensitivity[3]. Specifically, we used Alexa Fluor 488 (AF488) CTxB conjugates as the FRET donor and Alexa Fluor 647 (AF647) CTxB conjugates as the FRET acceptor. This pair has been previously established and validated, with a Förster critical distance (R_0) value around 52 Å[37]. The radius of the lipid domain determines how many CTxB probes can be accommodated within the same lipid domain. OMDs with a radius exceeding 10 nm have a high probability of accommodating multiple CTxB probes, whereas those with a radius smaller than 10 nm can only accommodate a single probe[3,36]. A higher FRET efficiency value is therefore indicative of a larger OMD size, allowing the CTxB FRET pair to detect relative changes in OMD size[3].

Live-cell time-resolved FLIM imaging was used to quantify FRET efficiency that reports OMD size in tsA-201 (a variant of HEK293T) cells[3]. The frequency-domain lifetime information corresponding to each pixel in the confocal image was transformed into a pixel on a complex plane coordinate, so-called phasor plot (Fig.1 a, b)[38]. This phasor plot displays a semicircular shape, which serves as a reference for pure single-exponential lifetimes[3,39]. Multiexponential lifetimes are found within the boundaries of this semicircle. Shorter lifetimes exhibit clockwise movements along the semicircle, indicating increased FRET. This phasor approach has several advantages, such as unbiased measurement of fluorescence lifetimes without the need for exponential fitting, and the ability to map multiple cursors to identify distinct lifetime species[38,40-42]. With the addition of both FRET donor (CTxB-AF488) and acceptor (CTxB-AF647), there was a clockwise shift towards a shorter lifetime compared to the donor-only lifetime, indicating the occurrence of FRET (Fig. 1a). To calculate FRET efficiency, we used the FRET trajectory method on the phasor plot[39]. The FRET trajectory started at the zero FRET efficiency position, aligned with the donor-only cursor, and moved through the measured phasor species. As previously demonstrated and reproduced here[3], this CTxB-based FRET efficiency was 8.8 ± 1.1% for tsA-201 cells (Fig. 1 c, d).

We found that treatment with purified exoenzyme C3 transferase (1 μg/mL, > 4 hrs), a specific Rho inhibitor, significantly reduced CTxB-based FRET efficiency in tsA cells. C3 transferase, derived from *C. botulinum*, inhibits Rho GTPases through ADP-ribosylation of the effector-binding domain[43,44]. Following treatment, the FRET efficiency decreased to 3.5 ± 0.5% (Fig. 1 b-d), indicating a disruption or

dispersion of OMDs. To examine the effect of Rho activation, we applied CN03 (1 μg/mL, > 4 hrs), a Rho activator derived from bacterial cytotoxic necrotizing factor (CNF) toxins that deamidates residue Q63 in the switch II region of Rho GTPases[45,46]. This modification maintains Rho in a constitutively active state[45,46]. CN03 is specific to Rho and does not modify other Ras family GTPases like Rac and Cdc42[45,46]. CN03 treatment markedly increased FRET efficiency to 15.3 ± 0.9% (Fig. 1 c, d), suggesting larger OMDs. These effects probably depended on endogenous, plasma membrane–localized RhoA (P61586; intensity: 6.43), which has significant expression in HEK293 cells, according to data from ProteomicsDB[47]. Together, these results suggest that RhoA activity modulates OMD organization in tsA cells— its activation drives domain coalescence, whereas its inhibition causes domain shrinkage.

To further assess changes in OMD organization during Rho activation, we performed FLIM-FRET using L10-CFP and L10-YFP, a FRET pair that preferentially partitions into OMDs[3,48,49]. L10 refers to a probe derived from the first 10 amino acids of the Lck kinase, which contains two palmitoylation sites and targets to OMDs (Fig. 1e). Unlike the CTxB-based probes—where increased FRET reflected domain coalescence and a higher chance for CTxB to bind to the membrane—the L10-based system reports decreased FRET as an indicator of OMD expansion, due to increased spacing between OMD-anchored L10 probes as OMDs expand[3,48]. We observed that the L10-based FRET increased following Rho inhibitor treatment and decreased with Rho activator treatment (Fig. 1f), further supporting the role of RhoA activation in OMD expansion. As an additional test, we used the FRET pair S15-CFP and S15-YFP, which localize to disordered membrane regions outside of OMDs[3,48,49]. This is because the S15 probe contains only a single myristoylation site without palmitoylation sites (Fig. 1e). FLIM-FRET changes in the S15-based CFP/YFP pair were less pronounced following treatment with Rho activators or inhibitors, compared to the L10-based FRET changes, suggesting that Rho activity has a more indirect impact on disordered membrane regions (Fig. 1g).

Optogenetic activation of RhoA facilitates OMD coalescence

Pharmacological agents can have off-target effects on related GTPases such as RhoB and RhoC. We further used an improved Light-inducible Dimerization (iLID) system that activates RhoA specifically (Fig. 2)[5-7]. This improved optogenetic system has several advantages over chemical dimerization systems and previous versions of light-induced systems, including shorter onset kinetics, smaller size, and the ability to be turned on and off reversibly[6,50,51]. The iLID system is fast-inducible within seconds following blue light excitation and reverts to the dark state within minutes[5], with a high recruitment efficiency and a considerable localization to the plasma membrane once activated[7,50,52].

The iLID optogenetic system involves the optical stimulation of a RhoA-selective GEF (Fig. 2 a, b). Specifically, there is a blue light-dependent interaction between a protein SspB and its peptide binding target SsrA. The mCherry-tagged SspB is fused to a RhoA-selective GEF, in this case LARG[53], and SsrA is fused to the blue light sensitive LOV2 domain (iLID-Caax), which is targeted to the membrane via the Caax anchor motif[5]. Upon 488 nm light excitation, the LOV2 domain, specifically the J_α helix, changes conformation so that SsrA becomes available for binding by SspB[54]. This allows for LARG to translocate to the membrane and activate RhoA. LARG preferentially activates RhoA over RhoB and RhoC and does not activate other Rho family proteins[55]. We confirmed blue-light induced LARG translocation through visualization of increased membrane-localized mCherry fluorescence following photoactivation (Fig. 2b). The mCherry was translocated from the cytosol to the membrane quickly, with a time constant of ~10 seconds (Fig. 2c). FLIM-FRET between CTxB-AF488 and CTxB-AF647 was measured during global photoactivation of the cell. In this protocol, the 488 nm laser served a dual purpose: activating the optogenetic system and exciting the FRET donor CTxB-AF488. We found the FRET efficiency significantly increased following endogenous RhoA activation, on average around 4% (Fig. 2 d-f). There was an exponential increase that had a time constant of ~65 seconds (Fig. 2e). Control cells lacking LARG-mCherry-SspB (untransfected) or iLID-CaaX (no mCherry translocation upon photoactivation) exhibited only an average increase of 1% in FRET efficiency (Fig. 2f). In addition, control experiments performed in the absence of the FRET acceptor, but in the presence of the optogenetic system, revealed no change in the FRET donor (CTxB-AF488) lifetime upon light activation (Supplementary Fig. 1). These results indicate that activation of endogenous RhoA in tsA201 cells promotes the expansion of OMDs.

We also tested the iLID system and effects on OMDs using the L10-based FRET pairs in tsA cells. Like the CTxB experiments, photoactivation was applied using 445 nm light, which simultaneously activated the optogenetic system and excited the FRET donor L10-CFP. Upon RhoA activation, we observed a considerable 3.4 ± 0.2% decrease (n = 5) in FRET efficiency between coexpressed L10-CFP and L10-YFP, with a time constant of ~70 seconds—comparable to the kinetics of the FRET increase observed for CTxB-based FRET pairs (Fig. 2 g-j). Control cells lacking LARG-mCherry-SspB translocation showed little changes in FRET (Fig. 2i). In tsA cells expressing the optogenetic system and S15-CFP and S15-YFP FRET pairs, photoactivation induced no measurable change in S15-based FRET efficiency (change in FLIM-FRET efficiency = 0 ± 0.3%), indicating that the effects observed with the L10 pair are specific to changes in lipid-ordered domains (Fig. 2j). In summary, these complementary results support the conclusion that RhoA activation drives the rapid coalescence of OMDs.

Dependence of RhoA-mediated OMD coalescence on cytoskeleton and protein palmitoylation

Considering the prominent role of RhoA in cytoskeletal remodeling, we tested whether disrupting the actin cytoskeleton would affect OMD size and the action of RhoA. Treatment with latrunculin A (Lat-A, 5 μM, 10 min), a potent actin polymerization inhibitor[56], increased the baseline CTxB-based FRET efficiency in tsA cells but nearly abolished the RhoA-induced increase in FRET following optogenetic activation (Fig. 2 k-m). These results suggest that an intact actin cytoskeletal network is required to maintain OMD organization. Disruption of cytoskeletal support promotes coalescence of OMDs into larger ordered domains, thereby impairing the ability of RhoA to further promote OMD expansion (Fig. 2l).

Given the critical role of palmitoylation in OMD formation and related endocytosis functions[57-59], we tested whether increasing cellular palmitate levels and altering protein palmitoylation modulate RhoA's effects on OMDs. The tsA cells were treated with palmitate conjugated to bovine serum albumin (palmitate/BSA; 50 μM, 20 min). As a control, cells were treated with BSA alone under identical conditions. Palmitate/BSA treatment increased the baseline CTxB-based FRET efficiency compared to BSA controls, indicating enhanced lipid order and enlargement of OMDs (Fig. 2 k-l). In contrast, BSA alone slightly reduced baseline FRET efficiency, likely due to its scavenging effect on free fatty acids present in the culture medium (Fig. 2 k-l). These results suggest that incorporation of saturated fatty acids into the plasma membrane promotes the formation or stabilization of larger OMDs. In the optogenetic RhoA activation experiment, BSA treatment attenuated the RhoA-induced FRET increase, whereas palmitate/BSA treatment preserved the FRET response (Fig. 2m). Furthermore, pre-treatment with 2-bromopalmitate (2-BP; 100 μM, 1 h), a broad-spectrum inhibitor of protein palmitoylation, did not alter baseline FRET efficiency but abolished the RhoA-induced FRET increase (Fig. 2 k-m). These results indicate that protein palmitoylation is required for RhoA-dependent OMD coalescence.

RhoA activation modulates the OMD size and controls membrane excitability in nociceptor DRG neurons

We extended these findings to rat primary small-diameter dorsal root ganglion (DRG) neurons, which are nociceptors responsible for detecting noxious stimuli and are highly sensitive to changes in membrane composition[60,61]. These small DRG neurons are important for processing pain signals and possess larger OMDs than large-diameter DRG neurons and tsA cells[3]. The FRET efficiency in naïve small DRG neurons (control) was measured at 19.5 ± 2.0% (Fig. 3 a, b). For these neurons, prolonged exposure to C3 transferase (1 μg/mL, >4 hrs) led to a significant decrease in CTxB-based FRET efficiency

to 10.7 ± 0.6%, consistent with a reduction in OMD sizes (Fig. 3 a, b). Conversely, activating Rho signaling using CN03 failed to elevate FRET efficiency significantly (measured as 20.6 ± 1.6%). This suggests that OMDs in naïve nociceptors are already large, rendering further Rho-induced expansion undetectable by the CTxB-based FRET method. Then we measured the spontaneous action potential firing of naïve nociceptor DRG neurons (Fig. 3c). In control neurons, 40% exhibited spontaneous firing (n = 15), consistent with our previous report[3]. Spontaneous firing increased to 93% in Rho inhibitor-treated neurons (n = 15), whereas 45% of Rho activator-treated neurons exhibited firing (n = 11). These results suggest that, as in tsA cells, decreased RhoA activity reduces OMDs in naïve sensory neurons, likely modulating their excitability and signaling properties.

We next tested whether activating RhoA could restore OMD integrity in nociceptor DRG neurons isolated from rats subjected to spared nerve injury (SNI), a well-established model of neuropathic pain[62]. Small-diameter neurons from SNI animals exhibited significantly reduced CTxB-based FRET efficiency (5.9 ± 1.1%) (Fig. 3d), reflecting a disruption of OMDs typically associated with chronic injury and membrane hyperexcitability[3]. Treatment with Rho activator CN03 reversed this reduction, restoring FRET efficiency (16.6 ± 1.6%) toward levels observed in naïve and contralateral SNI neuron controls (Fig. 3d). These findings suggest that Rho signaling plays an essential role in preserving OMD architecture under pathological conditions and may offer a mechanism to stabilize membrane nanodomain organization in sensory neurons affected by nerve injury. Notably, this restoration of OMD size coincided with reduced spontaneous firing: only 43% of RhoA-activated SNI neurons exhibited spontaneous activity (n = 14), compared to 100% in hyperexcitable SNI controls (n = 17), consistent with our previous findings[3] (Fig. 3e). Additionally, current injection–evoked action potential firing was potentiated by Rho inhibition but showed minimal change upon Rho activation in naïve neurons (Fig. 3f). In contrast, treatment with the Rho activator markedly reduced current injection–evoked action potential firing in ipsilateral SNI neurons (Fig. 3h). These distinct effects are consistent with reduced OMD size in hyperexcitable pain states and with Rho activation acting to dampen neuronal hyperexcitability.

To assess how the actin cytoskeleton and protein palmitoylation regulate OMD organization and neuronal excitability in naïve and SNI nociceptors, we performed CTxB-based FRET measurements analogous to those used in tsA cells (Supplementary Fig. 2 a, b). Disruption of the actin network with Lat-A selectively rescued the reduced OMD size observed in SNI neurons, while having minimal effect on naïve neurons. Manipulation of palmitoylation, either by palmitate supplementation or inhibition with 2-BP, significantly altered OMD size, consistent with the idea that protein palmitoylation is required to maintain OMD integrity. Functionally, 2-BP treatment reduced OMD size in naïve DRG neurons and was

sufficient to induce neuronal hyperexcitability (Supplementary Fig. 2c). In contrast, 2-BP had little additional effect on SNI neurons, which already display both hyperexcitability and reduced OMD size (Supplementary Fig. 2 b, d). In ipsilateral SNI neurons, Rho activation failed to reduce elicited action potential firing in the presence of a subsequent Lat-A treatment, indicating that RhoA's effect depends on an intact cytoskeletal network (Supplementary Fig. 2d). Together, these results indicate that disruption of palmitoylation-dependent OMD organization is sufficient to induce hyperexcitability in naïve neurons, whereas remodeling of the actin cytoskeleton likely mediates the OMD restoration in SNI neurons.

RhoA regulates OMDs through cytoskeleton-dependent modulation of membrane lateral tension

To examine how RhoA-induced changes of OMDs are dependent on cell cytoskeleton network, we used the mechanosensitive fluorescent probe Flipper-TR, which reports lateral membrane tension through changes in its fluorescence lifetime[63,64] (Fig. 4a). Because actin cytoskeletal dynamics are closely coupled to membrane tension, this approach allows us to directly assess how RhoA-mediated cytoskeletal remodeling influences the property of the membrane. Flipper-TR senses membrane lateral tension through planarization: as membrane tension increases, the lipid bilayer becomes more rigid and tightly packed, forcing the dithienothiophene dimer of Flipper-TR to align planarly and restricting its rotation[63,64]. This restriction prevents rotational quenching and enhances fluorescence emission, resulting in an increase in fluorescence lifetime[63]. Thus, using phasor FLIM to quantify lifetime, Flipper-TR provides a nanoscale readout of mechanical forces across the plasma membrane (Fig. 4b). As a proof-of-principle experiment, we applied extracellular solutions with different osmolarity to tsA cells labeled with Flipper-TR. The phase lifetime ($\tau\phi$) of Flipper increased from 4.5 ± 0.1 ns (hypotonic solution at 154 mOsm) to 4.8 ± 0.05 ns (isotonic solution at 326 mOsm), and to 5.2 ± 0.1 ns (hypertonic solution at 493 mOsm) (Fig. 4c). Similar changes of Flipper lifetime were observed in naïve DRG neurons in response to osmotic changes (Fig. 4d).

Using FLIM imaging of Flipper-TR, we monitored changes in membrane tension during pharmacological and optogenetic activation of RhoA to test whether increased membrane tension accompanies OMD expansion (Fig. 4 and Supplementary Table 1). We found that, in naïve DRG neurons, treatment with Rho inhibitor reduced the lifetime of Flipper-TR, whereas treatment with Rho activator produced little effect, likely because the membrane order and tension in naïve DRG neurons were already high (Fig. 4e). Importantly, in the ipsilateral SNI DRG neurons, the baseline Flipper lifetime is shorter, as the cell membrane is in a low-tension state, compared to naïve and contralateral SNI neurons (Fig. 4f). Treatment with RhoA activator rescued the low membrane tension observed in the ipsilateral neurons,

bringing it close to the level of naïve or contralateral SNI neurons (Fig. 4f). Furthermore, optogenetic RhoA activation in tsA-201 cells substantially increased the Flipper lifetime, indicating that RhoA activation is directly linked to increased membrane tension (Fig. 4g). Presumably, elevated membrane lateral tension promotes OMD coalescence by minimizing the total line tension energy associated with phase boundaries[65]. Under these conditions, the increased energetic cost of maintaining extensive domain interfaces disfavors multiple small OMDs and instead stabilizes fewer, larger domains.

Consistent with the changes observed in OMD size, both the actin cytoskeleton and protein palmitoylation contribute to the regulation of membrane tension (Supplementary Fig. 3a). In naïve DRG neurons, 2-BP reduced Flipper lifetime, whereas disrupting the actin cytoskeleton with Lat-A had little effect. Conversely, in ipsilateral nociceptors from SNI rats, Lat-A increased membrane tension, while 2-BP failed to further reduce Flipper lifetime—consistent with the higher baseline tension in naïve neurons compared to SNI neurons. Finally, RhoA activator pretreatment-induced increases in membrane tension were abolished by cytoskeletal disruption, indicating that an intact actin network is required for RhoA's effect (Supplementary Fig. 3a). In contrast, in ipsilateral SNI neurons, 2-BP did not prevent the RhoA activator–induced increase in membrane tension, suggesting that palmitoylation acts upstream of RhoA signaling rather than directly controlling this tension response (Supplementary Fig. 3a). Moreover, we assessed the effects of the chemotherapeutic agent paclitaxel, which has been reported to markedly reduce OMD size[3]. Because paclitaxel stabilizes microtubules, we hypothesized that it would elicit effects distinct from those of Lat-A-mediated actin disruption. Overnight treatment with 1 μM paclitaxel reduced the Flipper lifetime in naïve DRG neurons, indicating a reduced membrane tension. Paclitaxel had no effect on ipsilateral SNI neurons, where OMDs were constitutively disrupted and membrane tension was already low (Supplementary Fig. 3b). These results suggest that RhoA activation increases membrane tension through actin disruption, whereas microtubule stabilization produces the opposite effect. Lastly, as predicted, cholesterol depletion with methyl-β-cyclodextrin (MβCD) reduced membrane lateral tension in naïve DRG neurons, consistent with cholesterol's role in maintaining membrane rigidity (Supplementary Fig. 3c).

Rho activation modulates HCN channel function as a readout of OMD expansion

Beyond their essential role in supporting autonomous neuronal firing, the gating of hyperpolarization-activated cyclic nucleotide-modulated (HCN) channels is sensitive to lipid compartmentalization, which makes them a functional reporter for detecting alterations in OMD[3,66]. Disruption of OMDs—such as by cholesterol depletion using β-cyclodextrin (β-CD)—has been shown to markedly facilitate HCN channel gating, leading to faster activation and increased channel opening[3]. These changes in HCN gating contribute to enhanced neuronal excitability and are characteristic of sensory neurons under chronic neuropathic pain conditions[3,15]. In this context, we tested the role of RhoA signaling in modulating HCN channel function via OMDs. Using whole-cell patch clamp recordings, we measured native HCN currents in small-diameter DRG neurons from SNI rats by applying a series of hyperpolarizing voltage steps. To evaluate the role of RhoA signaling, we pharmacologically activated RhoA using CN03 and compared properties of HCN currents from treated and untreated controls (Fig. 5a). Ipsilateral nociceptor SNI neurons are known to exhibit disrupted OMDs and facilitated HCN channel opening, which contribute to their increased spontaneous activity[3]. We found treatment with the Rho activator (1 μg/mL, >4 hours) partially reversed this pathological phenotype. HCN channel activation kinetics were markedly slowed, with the primary activation time constant (τ_1) increasing from 75 ± 3 ms to 96 ± 6 ms (Fig. 5b). Although the half-maximal voltage ($V_{1/2}$) for channel activation derived from the conductance-voltage (G-V) curve did not change (Fig. 5c), the slope factor of the G-V curve was significantly reduced, consistent with a restoration of OMDs in nociceptor DRG neurons (Fig. 5d). The reduced slope factor suggests increased total gating charge movement per channel during activation, consistent with membrane thickening caused by OMD coalescence[3]. These findings demonstrate that RhoA activation supports OMD integrity, inhibits HCN channel function, and attenuates neuropathic hyperexcitability.

To further support the OMD-mediated effect on HCN channels by RhoA, we investigated whether inhibition of RhoA might alter the channel gating in the opposite direction for naïve small DRG neurons. As expected, we found that inhibiting RhoA with C3 transferase (1 μg/mL for ~4 hours) significantly accelerated HCN channel activation and increased the slope factor associated with the G-V activation curve (Fig. 5 e-g), recapitulating the β-CD-induced phenomenon of OMD disruption. Together, these results demonstrate that RhoA signaling critically stabilizes OMDs to regulate HCN gating and modulate action potential firing patterns.

A model for OMD coalescence driven by increased membrane lateral tension

To more directly test the hypothesis that membrane lateral tension promotes OMD coalescence directly—and to examine whether RhoA modulates OMD size without necessarily increasing total OMD area—we applied hypotonic treatment to cells (tsA cells and ipsilateral SNI DRG neurons) that display low CTxB-based FRET and relatively small OMDs. Acute hypotonic (154 mOsm) treatment mimicked the effects of RhoA activation, increasing OMD size as indicated by enhanced FRET efficiency (Supplementary Fig. 4), which arises from a higher probability of multiple CTxB molecules occupying the same OMD as coalescence occurs under elevated lateral tension[15]. In contrast, hypotonic treatment did not significantly increase FRET in contralateral SNI neurons, which already exhibit relatively large OMDs at baseline. Together, these findings provide additional evidence that RhoA-driven OMD coalescence is mediated by increased membrane lateral tension.

In neuropathic pain neurons, reduced membrane lateral tension leads to a decrease in OMD size (Fig. 5h). This change initiates signaling events that activate RhoA, which remodels the actin cytoskeleton to increase membrane lateral tension and restore OMD size (Fig. 5i). The resulting restoration suppresses HCN channel activity and modulates other ion channels, thereby reducing neuronal hyperexcitability (Fig. 5i). Consistent with these cellular effects, intraplantar injection of the RhoA activator attenuated mechanical hypersensitivity in the SNI pain model (Supplementary Fig. 5), in agreement with the in vitro findings.

Discussion

OMDs function to spatially compartmentalize membrane proteins, thereby regulating their interactions and activity[8]. Disturbances in OMD size, whether that be shrinking or expansion, have been linked to Alzheimer's disease[11,12], autoimmune disorders[8,14], and neuropathic pain[3,15]. We previously showed that OMDs regulate the excitability of nociceptive DRG neurons, with smaller OMDs enhancing membrane excitability and increasing action potential firing. In this study, we uncover a previously unknown link between the GTPase RhoA and neuropathic pain by examining how RhoA modulates OMDs. Using FLIM-FRET with OMD-specific probes, we achieved nanoscale resolution to track relative changes in OMD size and found that RhoA activation markedly expanded OMDs and restored membrane tension, establishing its direct regulatory role in OMD architecture.

We propose that during nerve injury and axon regeneration, RhoA activation serves as a key protective mechanism against neuronal hyperexcitability by modulating OMDs. Previously, RhoA activation was reported to influence membrane excitability by regulating the trafficking of voltage-gated ion channels[67-69]. RhoA activation was also suggested to interact with IP_3 receptors to modulate calcium signaling and the function of endothelial cells[70]. Nevertheless, the impact of RhoA activation specifically on nociceptor DRG neurons via ion channels has not been well studied. Our findings suggest that, beyond RhoA's established role in ion channel trafficking, direct RhoA/OMD-mediated attenuation of HCN channel gating may further contribute to decreased excitability in the soma of DRG neurons upon RhoA activation. Furthermore, RhoA activation following nerve injury likely halts axon regeneration and restricts damage to the injured region to conserve energy for soma survival[22,71], while simultaneously reducing somatic firing and alleviating the pain phenotype.

Our results support that RhoA activation promotes OMD coalescence through cytoskeletal remodeling and post-translational protein palmitoylation as underlying mechanisms. RhoA, a key regulator of actin cytoskeleton dynamics and stress fiber formation, modulates actomyosin contractility and cortical tension[18,21]. In neuropathic neurons, reduced membrane surface tension—likely at least in part resulting from cholesterol loss[15]—may feedback to activate RhoA[4], driving the coalescence of membrane domains into larger, more stable OMDs while concurrently restoring membrane tension. We also postulate that RhoA's facilitation of OMD coalescence may be dependent on palmitoylated proteins that preferentially localize to OMDs, such as GPI-anchored proteins, CD marker proteins, such as CD44[72,73], caveolins, and ion channels. S-palmitoylation facilitates the localization of membrane proteins to OMDs[57,59], and RhoA may reorganize the OMD localization of palmitoylated proteins by remodeling

the cytoskeleton[58,74,75]. Additionally, RhoA activity likely regulates the subcellular localization or activity of palmitoyl acyltransferases that contain DHHC domains, thereby influencing the lipidation status of OMD-residing proteins[58,76]. Moreover, our findings support the hypothesis that RhoA plays a critical role in the clathrin/dynamin-independent, OMD-dependent form of endocytosis first described by Hilgemann and colleagues[29-31]. Notably, the actin cytoskeleton appears dispensable in the late stages of OMDE, suggesting that lipid compartmentalization and membrane tension dominate vesicle formation[31]. Altogether, these findings imply that RhoA acts as a molecular bridge between cytoskeletal forces, membrane tension, and lipid domain dynamics, coordinating mechanical and biochemical cues that promote membrane domain formation and endocytosis events.

Our results support a model in which membrane lateral tension is a central biophysical determinant of plasma membrane lipid compartmentalization. Rather than increasing the total abundance of ordered lipids, pathways that elevate membrane tension, such as RhoA-dependent regulation of cortical actomyosin, appear to remodel membrane compartmentalization by promoting pre-existing nanoscale domains to merge into larger assemblies. From a biophysical standpoint, increased lateral tension reduces the energetic penalty associated with domain boundaries, thereby favoring coalescence of OMDs without necessitating net changes in membrane composition. Acute hypotonic swelling, which increases membrane tension, was sufficient to mimic the effects of RhoA activation. More broadly, these results suggest that signaling pathways that regulate membrane tension can dynamically remodel nanoscale membrane heterogeneity, directly impacting the spatial organization of membrane proteins and neuronal excitability.

Methods

Molecular Reagents, Cell Culture, and Transfection

Frozen aliquots of tsA-201 cells (RRID: CVCL_2737), a type of human embryonic kidney (HEK) cell commonly used for studying membrane ion channels and electrophysiology, were acquired from Sigma-Aldrich (St. Louis, MO) and stored in liquid nitrogen. Cells were cultured in Dulbecco's modified Eagle's medium (DMEM; Gibco), supplemented with 10% fetal bovine serum (FBS; Gibco) and 1% penicillin/streptomycin (Gibco), then stored in a humidified incubator at 37 degrees Celsius with 5% CO_2. Transient transfection was performed on 50-90% confluent tsA-201 cells with the lipofectamine 3000 kit (Invitrogen, Carlsbad, CA, #L30000080). Mycoplasma testing was performed using the MycoFluor™ Mycoplasma Detection Kit (Invitrogen) and tested negative. The iLID system included LARG-mCherry-sspB (Addgene: #90459) and iLID-CaaX-ssrA (Addgene: #85680). DNA concentration was measured using a Nanodrop OneC spectrophotometer (Life Technologies, Grand Island, NY). The cholera toxin subunit B-Alexa Fluor™ 488 and 647 conjugates were purchased from ThermoFisher Scientific and administered to cultured cells at a concentration of 20 nM for 5-10 minutes[3]. L10-CFP, L10-YFP, S15-CFP, and S15-YFP are gifts from Prof. Bertil Hille (University of Washington, Seattle). The membrane-permeable Rho activator II and inhibitor I were all purchased from Cytoskeleton, Inc (Denver, CO). The Flipper-TR membrane tension sensor (#SC020) was from Spirochrome (University of Geneva, Switzerland). Latrunculin A was purchased from Thermofisher (#L12370), and 2-bromopalmitate (#21604) was purchased from Sigma (St. Louis, MO) and was prepared at 5:1 ratio mixed with fatty-acid free bovine serum albumin (#A8806, Sigma). BSA-palmitate was from Cayman Chemical (#29558; 6:1 fatty acid to BSA ratio).

Fluorescence Lifetime Measurement and confocal FLIM-FRET

Digital frequency-domain fluorescence lifetime imaging[39,77] was performed with a Q2 laser scanning confocal system equipped with a FastFLIM data acquisition module (ISS, Inc, Champaign, IL), and two hybrid PMT detectors (Model R10467-40, Hamamatsu USA, Bridgewater, NJ). An Olympus IX73 inverted microscope (Olympus America, Waltham, MA) is coupled to the confocal system. Both the frequency domain (instantaneous distortion-free phasor plotting) and time-domain decay information are included in the fluorescence lifetime measurements. Simultaneous two-color imaging was performed with dichroic cubes, one equipped with a 50/50 beam splitter and the other with various long-pass filters. A supercontinuum laser with a wavelength range of 410 to 900 nm, a repetition rate of 20 MHz, and a pulse

duration of 6 ps was used for fluorescence excitation. Specifically, AF-488 was excited at 488 nm and mCherry was excited at 561 nm. To detect the emission for AF-488 and mCherry, an emission cube filter consisting of a 525/40 nm filter for AF-488, a 552 nm long-pass dichroic mirror, and a 593/40 nm filter for mCherry was employed. To detect the emission for CFP and YFP, an emission filter cube with a 475/28 nm filter for CFP, a 495 nm long-pass dichroic mirror, and a 542/27 nm filter for YFP was used. Only the donor lifetime was measured for phasor FLIM-FRET either in the presence or absence of the FRET acceptor. Optogenetic activation was performed with a supercontinuum laser using 445 nm or 488 nm excitation. The lifetime imaging of Flipper-TR was using 488 nm excitation and emission was collected using the 593/40 nm filter.

Confocal images of 256 x 256 pixel frame were obtained under each experimental condition, with a 100 μm motorized variable pinhole and a pixel dwell time of 0.1- 0.4 ms. Acquired pixels were examined using the phasor plot. The VistaVision software (ISS, Inc., Champaign, IL) was used for image processing, display, and acquisition and allows for the specification of parameters such as pixel dwell time, image size, and resolution. The fitting algorithm and multi-phasor analysis were used for FLIM analysis. A median/gaussian smoothing filter and intensity-threshold filter were applied to enhance the display and analysis of membrane-localized lifetime species. Phasor FLIM can differentiate between signals originating from the background outside of the membrane and those within the membrane. The VistaVision software was used for determination of phase delays (φ) and modulation ratios (m) of the fluorescence signal in response to an oscillatory stimulus with a frequency of ω. Sine and cosine Fourier transforms of the phase histogram were performed, with consideration for the instrument response function (IRF) calibrated with Atto 425 (lifetime: 3.6 ns) and rhodamine 110 (lifetime: 4 ns) measured in solution, for 445 nm and 488 nm excitations, respectively. The FLIM imaging of Flipper-TR was calibrated using rhodamine B (lifetime: 1.68 ns).

The FRET trajectory function in the VistaVision software allowed for analysis of FLIM-FRET measurements [38]. Three parameters were adjusted to ensure accurate results and optimize the fitting trajectory through both the unquenched donor and donor species affected by FRET. These parameters include the background contribution in the donor sample, unquenched donor contribution in the FRET sample, and the background contribution in the FRET sample. Background levels for both the donor sample and FRET sample were typically under 4%, which corresponds with the very low emission intensity observed in untransfected cells.

Three buffer solutions were formulated to achieve specific osmolarity for Flipper experiments. A hypotonic buffer (154 mmol/kg) was prepared by dissolving 37 mM NaCl, 5 mM KCl, 1 mM $MgCl_2$, 2 mM $CaCl_2$, 10 mM D-(+)-Glucose, and 20 mM HEPES. An isotonic buffer (326 mmol/kg) was prepared similarly but with 137 mM NaCl. A hypertonic buffer was then made by adding 150 mM sucrose to the isotonic buffer composition, resulting in a final osmolality of 493 mmol/kg. The pH of all solutions was adjusted to 7.4, and they were subsequently sterile-filtered and stored at 4°C.

Animals and Dorsal Root Ganglion (DRG) Neuron Preparation

All procedures involving animals were approved by the Institutional Animal Care and Use Committee (IACUC) of Saint Louis University and adhered to the National Institutes of Health guidelines. Adult pathogen-free Sprague-Dawley rats (100 – 250 g, Envigo, Placentia, CA) were housed under a 12-hour light/dark cycle (lights on at 06:00 AM) in a temperature-controlled room (23 ± 3°C) with ad libitum access to food and water. All behavioral experiments were conducted by investigators blinded to treatment conditions.

Primary DRG neurons were isolated from naïve (100 g) or adult (200 – 250 g) rats subjected to nerve injury. Animals were deeply anesthetized, and the dorsal skin and underlying musculature were carefully dissected to expose the vertebral column. Dorsal root ganglia (DRGs) were isolated by removing the vertebral bone overlying the spinal cord, followed by excision and trimming of the DRG roots. Isolated DRGs were enzymatically digested in 3 mL of sterile, bicarbonate-free, serum-free DMEM (Catalog# 11965, Thermo Fisher Scientific, Waltham, MA) containing 3.125 mg/mL neutral protease (Catalog# LS02104, Worthington Biochemical Corp., Lakewood, NJ) and 5 mg/mL collagenase Type I (Catalog# LS004194, Worthington). Tissue digestion was carried out at 37°C for 45 minutes with gentle agitation. Following digestion, cells were centrifuged and resuspended in DRG culture medium consisting of DMEM supplemented with 10% fetal bovine serum, 30 ng/mL nerve growth factor, and 1% penicillin/streptomycin. Cells (~1.5×10^6) were plated onto 12-mm coverslips pre-coated with poly-D-lysine and laminin and maintained at 37°C in a humidified incubator with 5% CO_2 until experimentation.

Spared Nerve Injury (SNI) Surgery and Behavioral Testing

Rats were anesthetized using 5% isoflurane for induction and maintained at 2.5% during surgery. Animals were placed on a heating pad to maintain core body temperature, and areflexia was confirmed prior to incision. The surgical site on the right hindlimb was cleaned with chlorhexidine (applied twice),

and a 2–3 cm incision was made along the lateral thigh. The biceps femoris muscle was bluntly retracted to expose the sciatic nerve and its three terminal branches. The common peroneal and tibial nerves were tightly ligated using 4–0 silk sutures and transected, while the sural nerve was left intact. The muscle was closed with 5–0 absorbable suture, and the skin was closed with surgical clips. Topical antibiotic ointment was applied, and animals were allowed to recover for 10 days before behavioral assessments.

Von Frey mechanical sensitivity testing was used to assess tactile allodynia. Testing was conducted in a blinded manner in a quiet, temperature-controlled room. Rats were acclimated to the testing environment in individual Plexiglas chambers placed on a wire mesh platform. Calibrated von Frey filaments were applied to the lateral plantar surface of the hindpaw, and the 50% paw withdrawal threshold was determined using the up-down method.

Patch-Clamp Electrophysiology

Electrophysiological recordings were performed in whole-cell configuration using an EPC10 amplifier and PATCHMASTER software (HEKA Elektronik), with data acquired at a sampling rate of 5 kHz. Recording pipettes were pulled from borosilicate glass capillaries using a P1000 puller (Sutter Instruments, Novato, CA) and had a resistance of 2.5-4 MΩ when filled. Precise positioning of pipettes was achieved using a Sutter MP-225A motorized micromanipulator. All recordings were conducted at ambient room temperature.

To record HCN channel currents in dorsal root ganglion (DRG) neurons, the internal pipette solution contained (in mM): 10 NaCl, 137 KCl, 4 Mg-ATP, 10 HEPES, and 1 EGTA, pH adjusted to 7.3 with KOH. The inclusion of 4 mM Mg-ATP was sufficient to preserve intracellular phosphoinositide levels, particularly $PI(4,5)P_2$, throughout the duration of recordings (52, 53). The extracellular solution consisted of (in mM): 154 NaCl, 5.6 KCl, 1 $MgCl_2$, 1 $CaCl_2$, 8 HEPES, and 10 D-glucose, titrated to pH 7.4 with NaOH. Series resistance was routinely maintained below 10 MΩ and compensated by 40%–70%. For the action potential measurements, whole-cell current clamp mode of PATCHMASTER was used instead of the voltage-clamp configuration for HCN current measurements. Spontaneous firing was measured with 0 pA current injection. For the current injection-evoked action potential firing, membrane potential was initially held at -60 mV. During current injection, neurons exhibited firing that adapted at higher amplitudes, likely due to sodium channel inactivation.

HCN current activation properties were assessed by measuring tail currents at −60 mV, following a series of test voltages from −40 mV to −140 mV in 10 mV increments. Leak-subtracted tail currents were normalized to the maximal amplitude and plotted to generate conductance-voltage (G–V) relationships. These data were fitted with a Boltzmann function: $G/G_{max} = 1/(1 + \exp[(V - V_{1/2})/V_S])$, where V is the test potential, $V_{1/2}$ is the voltage at which half-maximal activation occurs, and V_S is the slope factor. The slope factor was defined as $V_S = RT/zeF$, where R is the gas constant, T is the absolute temperature (297 K), F is the Faraday constant, e is the elementary charge, and z is the effective gating charge.

Statistics and Reproducibility

The data parameters were presented as the mean ± s.e.m. of n independent cells. Statistical significance was determined using the two-sided student's t test for comparison of two groups, or a one-way ANOVA test followed by a Tukey's post hoc test for comparison of more than two groups, denoted as $^*p < 0.05$ and $^{**}p < 0.01$ respectively.

Acknowledgements

We thank Erin N. Lessie, Lyuba Salih, Gege Guzman, and Haya Alkhateeb for technical support, and Kyle S. McCommis for sharing chemicals. This research is supported by National Institute of General Medical Sciences R35GM154778 grant (to G.D.), R56HL169176 (to G.D.) and by the Doisy Fund (to G.D. and L.J.H.) of the Edward A. Doisy Department of Biochemistry and Molecular Biology at Saint Louis University School of Medicine. The Moutal lab is supported by startup funds from the Department of Pharmacology and Physiology, Saint Louis University, Institute for Drug & Biotherapeutic Innovation seed grant, National Institute of Neurological Disorders and Stroke R01NS119263 grant. Cartoons in figures were created using BioRender.

Author Contributions

G.D., A.M., and D.W.H. conceptualized and designed the research. S.S. and L.J.H. performed data acquisition and analysis for fluorescence imaging and electrophysiology, respectively. N.L.M. and G.D. performed pilot experiments for fluorescence imaging. A.M., C.G., and N.L.A.D. supervised and performed DRG neuron preparations and rat studies. G.D. wrote the manuscript.

Competing Interests

The authors declare no competing interests.

References

1 Lingwood, D. & Simons, K. Lipid rafts as a membrane-organizing principle. *Science* **327**, 46-50 (2010). https://doi.org:10.1126/science.1174621

2 Levental, I. & Lyman, E. Regulation of membrane protein structure and function by their lipid nano-environment. *Nat Rev Mol Cell Biol* **24**, 107-122 (2023). https://doi.org:10.1038/s41580-022-00524-4

3 Handlin, L. J. *et al.* Membrane lipid nanodomains modulate HCN pacemaker channels in nociceptor DRG neurons. *Nat Commun* **15**, 9898 (2024). https://doi.org:10.1038/s41467-024-54053-z

4 Bement, W. M., Goryachev, A. B., Miller, A. L. & von Dassow, G. Patterning of the cell cortex by Rho GTPases. *Nat Rev Mol Cell Biol* **25**, 290-308 (2024). https://doi.org:10.1038/s41580-023-00682-z

5 Guntas, G. *et al.* Engineering an improved light-induced dimer (iLID) for controlling the localization and activity of signaling proteins. *Proc Natl Acad Sci U S A* **112**, 112-117 (2015). https://doi.org:10.1073/pnas.1417910112

6 Inaba, H., Miao, Q. & Nakata, T. Optogenetic control of small GTPases reveals RhoA mediates intracellular calcium signaling. *J Biol Chem* **296**, 100290 (2021). https://doi.org:10.1016/j.jbc.2021.100290

7 O'Neill, P. R. *et al.* Membrane Flow Drives an Adhesion-Independent Amoeboid Cell Migration Mode. *Dev Cell* **46**, 9-22 e24 (2018). https://doi.org:10.1016/j.devcel.2018.05.029

8 Sezgin, E., Levental, I., Mayor, S. & Eggeling, C. The mystery of membrane organization: composition, regulation and roles of lipid rafts. *Nat Rev Mol Cell Biol* **18**, 361-374 (2017). https://doi.org:10.1038/nrm.2017.16

9 Lingwood, D. & Simons, K. Lipid Rafts as a Membrane-Organizing Principle. *Science* **327**, 46-50 (2010).

10 Veatch, S. L. & Keller, S. L. Organization in lipid membranes containing cholesterol. *Phys Rev Lett* **89**, 268101 (2002). https://doi.org:10.1103/PhysRevLett.89.268101

11 Ehehalt, R., Keller, P., Haass, C., Thiele, C. & Simons, K. Amyloidogenic processing of the Alzheimer beta-amyloid precursor protein depends on lipid rafts. *J Cell Biol* **160**, 113-123 (2003). https://doi.org:10.1083/jcb.200207113

12 Andrew, R. J. *et al.* Lack of BACE1 S-palmitoylation reduces amyloid burden and mitigates memory deficits in transgenic mouse models of Alzheimer's disease. *Proc Natl Acad Sci U S A* **114**, E9665-E9674 (2017). https://doi.org:10.1073/pnas.1708568114

13 Fecchi, K. *et al.* Coronavirus Interplay With Lipid Rafts and Autophagy Unveils Promising Therapeutic Targets. *Front Microbiol* **11**, 1821 (2020). https://doi.org:10.3389/fmicb.2020.01821

14 Varshney, P., Yadav, V. & Saini, N. Lipid rafts in immune signalling: current progress and future perspective. *Immunology* **149**, 13-24 (2016). https://doi.org:10.1111/imm.12617

15 Handlin, L. J. *et al.* Sequential Membrane Remodeling by Cholesterol Distinctly Modulates HCN Channels in Naive and Neuropathic DRG Neurons. *bioRxiv* (2025). https://doi.org:10.1101/2025.06.15.659789

16 Wennerberg, K., Rossman, K. L. & Der, C. J. The Ras superfamily at a glance. *J. Cell Sci.* **118**, 843-846 (2005).

17 Schaefer, A., Reinhard, N. R. & Hordijk, P. L. Toward understanding RhoGTPase specificity: structure, function and local activation. *Small GTPases* **5**, 6 (2014). https://doi.org:10.4161/21541248.2014.968004

18 Oakes, P. W. *et al.* Optogenetic control of RhoA reveals zyxin-mediated elasticity of stress fibres. *Nat Commun* **8**, 15817 (2017). https://doi.org:10.1038/ncomms15817

19 Ma, X., Zhao, Y., Daaka, Y. & Nie, Z. Acute activation of β2-adrenergic receptor regulates focal adhesions through βArrestin2- and p115RhoGEF protein-mediated activation of RhoA. *J Biol Chem* **287**, 18925-18936 (2012). https://doi.org:10.1074/jbc.M112.352260

20 Ridley, A. J. Rho family proteins: coordinating cell responses. *Trends Cell Biol* **11**, 471-477 (2001). https://doi.org:10.1016/s0962-8924(01)02153-5
21 Eckenstaler, R., Hauke, M. & Benndorf, R. A. A current overview of RhoA, RhoB, and RhoC functions in vascular biology and pathology. *Biochem Pharmacol* **206**, 115321 (2022). https://doi.org:10.1016/j.bcp.2022.115321
22 Cheng, C. *et al.* Activated RhoA and peripheral axon regeneration. *Exp Neurol* **212**, 358-369 (2008). https://doi.org:10.1016/j.expneurol.2008.04.023
23 Temporin, K. *et al.* IL-1β promotes neurite outgrowth by deactivating RhoA via p38 MAPK pathway. *Biochem Biophys Res Commun* **365**, 375-380 (2008). https://doi.org:10.1016/j.bbrc.2007.10.198
24 Lehmann, M. *et al.* Inactivation of Rho signaling pathway promotes CNS axon regeneration. *J Neurosci* **19**, 7537-7547 (1999). https://doi.org:10.1523/JNEUROSCI.19-17-07537.1999
25 Neumann, H. *et al.* Tumor necrosis factor inhibits neurite outgrowth and branching of hippocampal neurons by a rho-dependent mechanism. *J Neurosci* **22**, 854-862 (2002). https://doi.org:10.1523/JNEUROSCI.22-03-00854.2002
26 Hu, J. & Selzer, M. E. RhoA as a target to promote neuronal survival and axon regeneration. *Neural Regen Res* **12**, 525-528 (2017). https://doi.org:10.4103/1673-5374.205080
27 Quarta, S. *et al.* Sphingosine-1-Phosphate and the S1P(3) Receptor Initiate Neuronal Retraction via RhoA/ROCK Associated with CRMP2 Phosphorylation. *Front Mol Neurosci* **10**, 317 (2017). https://doi.org:10.3389/fnmol.2017.00317
28 Kranenburg, O. *et al.* Activation of RhoA by lysophosphatidic acid and $G\alpha_{12/13}$ subunits in neuronal cells: induction of neurite retraction. *Mol Biol Cell* **10**, 1851-1857 (1999). https://doi.org:10.1091/mbc.10.6.1851
29 Hilgemann, D. W. *et al.* Lipid signaling to membrane proteins: From second messengers to membrane domains and adapter-free endocytosis. *J Gen Physiol* **150**, 211-224 (2018). https://doi.org:10.1085/jgp.201711875
30 Lariccia, V. *et al.* Massive calcium-activated endocytosis without involvement of classical endocytic proteins. *J Gen Physiol* **137**, 111-132 (2011). https://doi.org:10.1085/jgp.201010468
31 Hilgemann, D. W., Lin, M. J., Fine, M. & Deisl, C. On the existence of endocytosis driven by membrane phase separations. *Biochim Biophys Acta Biomembr* **1862**, 183007 (2020). https://doi.org:10.1016/j.bbamem.2019.06.006
32 Deisl, C., Moe, O. W. & Hilgemann, D. W. Constitutive Plasma Membrane Turnover in T-REx293 cells via Ordered Membrane Domain Endocytosis under Mitochondrial Control. *bioRxiv* (2024). https://doi.org:10.1101/2024.01.17.576124
33 Laguia, F. *et al.* Massive endocytosis mechanisms are involved in uptake of HIV-1 particles by monocyte-derived dendritic cells. *Front Immunol* **15**, 1505840 (2024). https://doi.org:10.3389/fimmu.2024.1505840
34 Hilgemann, D. W. & Fine, M. Mechanistic analysis of massive endocytosis in relation to functionally defined surface membrane domains. *J Gen Physiol* **137**, 155-172 (2011). https://doi.org:10.1085/jgp.201010470
35 Matsubara, T. *et al.* Heterogeneous Ganglioside-Enriched Nanoclusters with Different Densities in Membrane Rafts Detected by a Peptidyl Molecular Probe. *Langmuir* **37**, 646-654 (2021).
36 Sachl, R. *et al.* On multivalent receptor activity of GM1 in cholesterol containing membranes. *Biochim Biophys Acta* **1853**, 850-857 (2015). https://doi.org:10.1016/j.bbamcr.2014.07.016
37 Huang, F. *et al.* Multiple conformations of full-length p53 detected with single-molecule fluorescence resonance energy transfer. *Proc Natl Acad Sci U S A* **106**, 20758-20763 (2009). https://doi.org:10.1073/pnas.0909644106
38 Digman, M. A., Caiolfa, V. R., Zamai, M. & Gratton, E. The phasor approach to fluorescence lifetime imaging analysis. *Biophys J* **94**, L14-16 (2008). https://doi.org:10.1529/biophysj.107.120154

39 Handlin, L. J. & Dai, G. Direct regulation of the voltage sensor of HCN channels by membrane lipid compartmentalization. *Nat Commun* **14**, 6595 (2023). https://doi.org:10.1038/s41467-023-42363-7
40 Hinde, E., Digman, M. A., Hahn, K. M. & Gratton, E. Millisecond spatiotemporal dynamics of FRET biosensors by the pair correlation function and the phasor approach to FLIM. *Proc Natl Acad Sci U S A* **110**, 135-140 (2013). https://doi.org:10.1073/pnas.1211882110
41 Malacrida, L., Ranjit, S., Jameson, D. M. & Gratton, E. The Phasor Plot: A Universal Circle to Advance Fluorescence Lifetime Analysis and Interpretation. *Annu Rev Biophys* **50**, 575-593 (2021). https://doi.org:10.1146/annurev-biophys-062920-063631
42 Ranjit, S., Malacrida, L., Jameson, D. M. & Gratton, E. Fit-free analysis of fluorescence lifetime imaging data using the phasor approach. *Nat Protoc* **13**, 1979-2004 (2018). https://doi.org:10.1038/s41596-018-0026-5
43 Wilde, C., Genth, H., Aktories, K. & Just, I. Recognition of RhoA by Clostridium botulinum C3 exoenzyme. *J Biol Chem* **275**, 16478-16483 (2000). https://doi.org:10.1074/jbc.M910362199
44 Just, I. *et al.* Purification and characterization of an ADP-ribosyltransferase produced by Clostridium limosum. *J Biol Chem* **267**, 10274-10280 (1992).
45 Flatau, G. *et al.* Toxin-induced activation of the G protein p21 Rho by deamidation of glutamine. *Nature* **387**, 729-733 (1997). https://doi.org:10.1038/42743
46 Schmidt, G. *et al.* Gln 63 of Rho is deamidated by Escherichia coli cytotoxic necrotizing factor-1. *Nature* **387**, 725-729 (1997). https://doi.org:10.1038/42735
47 Schmidt, T. *et al.* ProteomicsDB. *Nucleic Acids Res* **46**, D1271-D1281 (2018). https://doi.org:10.1093/nar/gkx1029
48 Myeong, J., Park, C. G., Suh, B. C. & Hille, B. Compartmentalization of phosphatidylinositol 4,5-bisphosphate metabolism into plasma membrane liquid-ordered/raft domains. *Proc Natl Acad Sci U S A* **118** (2021). https://doi.org:10.1073/pnas.2025343118
49 Chichili, G. R. & Rodgers, W. Clustering of membrane raft proteins by the actin cytoskeleton. *J Biol Chem* **282**, 36682-36691 (2007). https://doi.org:10.1074/jbc.M702959200
50 Mahlandt, E. K. *et al.* Opto-RhoGEFs, an optimized optogenetic toolbox to reversibly control Rho GTPase activity on a global to subcellular scale, enabling precise control over vascular endothelial barrier strength. *Elife* **12** (2023). https://doi.org:10.7554/eLife.84364
51 Wagner, E. & Glotzer, M. Local RhoA activation induces cytokinetic furrows independent of spindle position and cell cycle stage. *J Cell Biol* **213**, 641-649 (2016). https://doi.org:10.1083/jcb.201603025
52 Benedetti, L. *et al.* Light-activated protein interaction with high spatial subcellular confinement. *Proc Natl Acad Sci U S A* **115**, E2238-E2245 (2018). https://doi.org:10.1073/pnas.1713845115
53 Kristelly, R., Gao, G. & Tesmer, J. J. Structural determinants of RhoA binding and nucleotide exchange in leukemia-associated Rho guanine-nucleotide exchange factor. *J Biol Chem* **279**, 47352-47362 (2004). https://doi.org:10.1074/jbc.M406056200
54 Iuliano, J. N. *et al.* Unraveling the Mechanism of a LOV Domain Optogenetic Sensor: A Glutamine Lever Induces Unfolding of the Jalpha Helix. *ACS Chem Biol* **15**, 2752-2765 (2020). https://doi.org:10.1021/acschembio.0c00543
55 Jaiswal, M., Dvorsky, R. & Ahmadian, M. R. Deciphering the molecular and functional basis of Dbl family proteins: a novel systematic approach toward classification of selective activation of the Rho family proteins. *J Biol Chem* **288**, 4486-4500 (2013). https://doi.org:10.1074/jbc.M112.429746
56 Coue, M., Brenner, S. L., Spector, I. & Korn, E. D. Inhibition of actin polymerization by latrunculin A. *FEBS Lett* **213**, 316-318 (1987). https://doi.org:10.1016/0014-5793(87)81513-2
57 Levental, I., Lingwood, D., Grzybek, M., Coskun, U. & Simons, K. Palmitoylation regulates raft affinity for the majority of integral raft proteins. *Proc Natl Acad Sci U S A* **107**, 22050-22054 (2010). https://doi.org:10.1073/pnas.1016184107

58 Hilgemann, D. W., Fine, M., Linder, M. E., Jennings, B. C. & Lin, M. J. Massive endocytosis triggered by surface membrane palmitoylation under mitochondrial control in BHK fibroblasts. *Elife* **2**, e01293 (2013). https://doi.org:10.7554/eLife.01293
59 Lin, M. J. *et al.* Massive palmitoylation-dependent endocytosis during reoxygenation of anoxic cardiac muscle. *Elife* **2**, e01295 (2013). https://doi.org:10.7554/eLife.01295
60 Esposito, M. F., Malayil, R., Hanes, M. & Deer, T. Unique Characteristics of the Dorsal Root Ganglion as a Target for Neuromodulation. *Pain Med* **20**, S23-S30 (2019). https://doi.org:10.1093/pm/pnz012
61 Cheng, H., Jiang, X. & Han, X. Alterations in lipid homeostasis of mouse dorsal root ganglia induced by apolipoprotein E deficiency: a shotgun lipidomics study. *J Neurochem* **101**, 57-76 (2007). https://doi.org:10.1111/j.1471-4159.2006.04342.x
62 Decosterd, I. & Woolf, C. J. Spared nerve injury: an animal model of persistent peripheral neuropathic pain. *Pain* **87**, 149-158 (2000). https://doi.org:10.1016/S0304-3959(00)00276-1
63 Colom, A. *et al.* A fluorescent membrane tension probe. *Nat Chem* **10**, 1118-1125 (2018). https://doi.org:10.1038/s41557-018-0127-3
64 Dal Molin, M. *et al.* Fluorescent flippers for mechanosensitive membrane probes. *J Am Chem Soc* **137**, 568-571 (2015). https://doi.org:10.1021/ja5107018
65 Akimov, S. A., Kuzmin, P. I., Zimmerberg, J. & Cohen, F. S. Lateral tension increases the line tension between two domains in a lipid bilayer membrane. *Phys Rev E* **75** (2007). https://doi.org:10.1103/PhysRevE.75.011919
66 Robinson, R. B. & Siegelbaum, S. A. Hyperpolarization-activated cation currents: from molecules to physiological function. *Annu Rev Physiol* **65**, 453-480 (2003). https://doi.org:10.1146/annurev.physiol.65.092101.142734
67 Stirling, L., Williams, M. R. & Morielli, A. D. Dual roles for RHOA/RHO-kinase in the regulated trafficking of a voltage-sensitive potassium channel. *Mol Biol Cell* **20**, 2991-3002 (2009). https://doi.org:10.1091/mbc.e08-10-1074
68 Pochynyuk, O., Staruschenko, A., Bugaj, V., Lagrange, L. & Stockand, J. D. Quantifying RhoA facilitated trafficking of the epithelial Na+ channel toward the plasma membrane with total internal reflection fluorescence-fluorescence recovery after photobleaching. *J Biol Chem* **282**, 14576-14585 (2007). https://doi.org:10.1074/jbc.M701348200
69 Rousset, M. *et al.* Regulation of neuronal high-voltage activated Ca_V2 Ca^{2+} channels by the small GTPase RhoA. *Neuropharmacology* **97**, 201-209 (2015). https://doi.org:10.1016/j.neuropharm.2015.05.019
70 Mehta, D. *et al.* RhoA interaction with inositol 1,4,5-trisphosphate receptor and transient receptor potential channel-1 regulates Ca^{2+} entry. Role in signaling increased endothelial permeability. *J Biol Chem* **278**, 33492-33500 (2003). https://doi.org:10.1074/jbc.M302401200
71 Stern, S. *et al.* RhoA drives actin compaction to restrict axon regeneration and astrocyte reactivity after CNS injury. *Neuron* **109**, 3436-3455 e3439 (2021). https://doi.org:10.1016/j.neuron.2021.08.014
72 Vogl, D. P. *et al.* Semisynthesis of segmentally isotope-labeled and site-specifically palmitoylated CD44 cytoplasmic tail. *Bioorg Med Chem* **100**, 117617 (2024). https://doi.org:10.1016/j.bmc.2024.117617
73 Yu, X. *et al.* Mechano-crosstalk between living and artificial cells. *Nat Commun* **16**, 8582 (2025). https://doi.org:10.1038/s41467-025-63581-1
74 Rocks, O. *et al.* An acylation cycle regulates localization and activity of palmitoylated Ras isoforms. *Science* **307**, 1746-1752 (2005). https://doi.org:10.1126/science.1105654
75 Navarro-Lerida, I. *et al.* A palmitoylation switch mechanism regulates Rac1 function and membrane organization. *EMBO J* **31**, 534-551 (2012). https://doi.org:10.1038/emboj.2011.446
76 Fukata, Y., Murakami, T., Yokoi, N. & Fukata, M. Local Palmitoylation Cycles and Specialized Membrane Domain Organization. *Curr Top Membr* **77**, 97-141 (2016). https://doi.org:10.1016/bs.ctm.2015.10.003

77 Colyer, R. A., Lee, C. & Gratton, E. A novel fluorescence lifetime imaging system that optimizes photon efficiency. *Microsc Res Tech* **71**, 201-213 (2008). https://doi.org:10.1002/jemt.20540

Figure Legends

Fig. 1. Rho activation increases the OMD size quantified using FLIM-FRET.

a-b, Representative phasor plot of tsA-201 cells labeled by CTxB-AF488 and CTxB-AF647, without (a) and with (b) treatment of Rho inhibitor. The donor alone phasor is indicated as the green cursor, obtained from cells only labeled with CTxB-AF488. The trajectory curve in red begins at 0% FRET efficiency (donor only), progresses through the measured phasor, and ends at 100% efficiency, which overlaps with the background (0,0) coordinate. **c**, Representative FLIM-FRET based heatmap images of tsA cells illustrate the effects of Rho inhibitor and activator on the CTxB-based FLIM-FRET efficiency. **d**, Summary of effects of Rho inhibitor and activator on the CTxB-based FLIM-FRET efficiency in tsA cells as shown in panel c, n = 8 for the untreated control, n = 13 for the Rho inhibitor, and n = 7 for the Rho activator. Data are mean ± s.e.m., **P < 0.01, one-way ANOVA (no adjustment). **e**, Schematic illustration of L10- and S15-CFP probes. AlphaFold 3-generated structures of the first 10 residues of L10 and the first 15 residues of S15 are also shown. **f-g**, Summary of analogous experiments testing the Rho inhibitor and activator on the L10-based (n = 7 – 11 cells, panel f) or S15-based (n = 4 – 6 cells, panel g) FLIM-FRET efficiency in tsA cells. Data are mean ± s.e.m., *P < 0.05, one-way ANOVA (no adjustment).

Fig. 2. Activation of RhoA using an improved light-inducible dimerization (iLID) system.

a, Schematic of the iLID module before and after 488-nm illumination. Photoexcitation triggers a conformational change in LOV2–Caax–SsrA that exposes the SsrA motif and enables SspB binding. **b**, Intensity-based heatmaps of tsA-201 cells before and after illumination show that activation of the iLID system drives rapid redistribution of LARG–mCherry from the cytosol to the plasma membrane. Line-scan profiles confirm increased membrane-associated fluorescence concurrent with reduced cytosolic signal. **c**, Time course of LARG–mCherry recruitment quantified as the ratio of membrane-localized to cytosolic fluorescence (n = 4 cells). **d**, Representative phasor plots from cells labeled with CTxB-AF488 and CTxB-AF647 and expressing the iLID module. Comparison of the start and the end of 488-nm excitation reveals an increase in FRET efficiency, consistent with enhanced lipid order. **e**, Corresponding time course of FLIM-FRET efficiency between CTxB-AF488 and CTxB-AF647. **f**, Summary of CTxB-based FRET changes in cells exhibiting clear LARG–mCherry translocation versus those lacking detectable recruitment (mean ± s.e.m.; n = 8; **P < 0.01, two-sided t-test). **g**, Representative phasor plots from cells expressing L10-CFP/YFP and the iLID module. **h-i**, Time course of L10-based FRET during 445-nm illumination in cells with (h) or without (i) LARG–mCherry membrane recruitment, demonstrating that iLID-evoked changes in membrane order are tightly coupled to RhoA activation. **j**, Summary of L10- and S15-based FRET responses in cells with or without LARG–mCherry translocation (L10: n = 13 without, n = 5 with; S15: n = 10 without, n = 8 with; **P < 0.01, one-way ANOVA). **k**, Representative

FLIM–FRET heatmaps of CTxB-labeled tsA cells under control conditions or following treatment with Lat-A, palmitate, or 2-BP, illustrating how cytoskeletal disruption or altered palmitoylation modulates baseline membrane order. **l**, Quantification of baseline CTxB-based FRET efficiencies for control (n = 13), Lat-A (n = 11), BSA (n = 10), palmitate (n = 12), and 2-BP (n = 7) conditions (**P < 0.01, two-sided t-test). **m**, Summary of iLID-evoked changes in CTxB-based FRET across the same pharmacological conditions (control: n = 8, Lat-A: n = 6, BSA: n = 9, palmitate: n = 9, 2-BP: n = 6; **P < 0.01, one-way ANOVA).

Fig. 3. RhoA-dependent regulation of membrane order and excitability in small DRG neurons.
a, Representative FLIM–FRET heatmaps of naïve small-diameter DRG neurons labeled with CTxB illustrate the reduction in membrane-order–dependent FRET efficiency following acute Rho inhibition. **b**, Quantification of CTxB-based FLIM–FRET efficiencies in naïve neurons under control conditions (n = 11 cells), after Rho inhibition (n = 6), or after Rho activation (n = 9) (mean ± s.e.m.; one-way ANOVA). **c**, Pie charts showing the proportion of naïve DRG neurons exhibiting spontaneous action potential (AP) firing in control versus Rho inhibitor–treated groups (green, spontaneous APs; red, silent). **d**, Summary of CTxB-based FLIM–FRET efficiencies in small DRG neurons from spared nerve injury (SNI) rats. Ipsilateral neurons showed increased FRET after Rho activation (control: n = 9 cells; Rho activator: n = 13). Corresponding data for contralateral neurons are shown (control: n = 11 cells; Rho activator: n = 10) (one-way ANOVA, p = 2e-6 for the ipsilateral neurons and p = 0.27 for contralateral neurons). **e**, Pie charts illustrating the fraction of ipsilateral SNI neurons that fired spontaneous APs under control conditions versus after Rho activation. **f**, Representative traces of current injection–evoked AP firing in naïve nociceptors under control conditions and after Rho inhibition, highlighting enhanced excitability with suppressed RhoA activity. **g**, Summary of current injection-elicited AP firing in naïve DRG neurons under control conditions (n = 13 patches), with Rho inhibition (n = 7), or with Rho activation (n = 9). AP counts are plotted against injected current steps (mean ± s.e.m., p = 0.02 at 40 pA and p = 0.005 at 60 pA; one-way ANOVA). **h**, Summary of current injection-evoked firing from ipsilateral SNI nociceptors under control conditions (n = 15 patches) and after overnight Rho activation (n = 8), two-sided t-test, *p < 0.05, **p < 0.01.

Fig. 4. RhoA-dependent modulation of membrane tension measured by the sensor Flipper.
a, Schematic of FLIM imaging of the mechanosensitive probe Flipper, which reports local membrane surface tension via changes in fluorescence lifetime. The dithienothiophene rings of Flipper planarize under increased membrane tension, restricting rotational freedom and increasing fluorescence lifetime. Flipper-TR has an additional head group (not shown) for plasma membrane localization. **b**. Representative Flipper-TR lifetime-based heatmap images of tsA cells exposed to extracellular solutions

of varying osmolarity, showing graded increases from hypotonic to isotonic and hypertonic conditions, as well as the lifetime shift shown in the phasor plot. **c**-**d**, Summary of osmolarity-dependent lifetime changes in tsA cells (c) and naïve DRG neurons (d). n = 7-9 cells for tsA and n = 6-16 for naïve DRG, mean ± s.e.m., one-way ANOVA (no adjustment). **e**, Pharmacological manipulation of RhoA activity in naïve DRG neurons revealed that Rho inhibition lowered Flipper-TR lifetime, whereas Rho activation produced minimal effects, n = 12 for the control and Rho inhibitor; n = 13 for Rho activator, mean ± s.e.m., one-way ANOVA (no adjustment). **f**, Summary data of SNI DRG neurons that exhibited reduced baseline lifetimes indicative of low membrane tension, RhoA activation substantially increased lifetime, restoring values toward those of contralateral neurons, n = 13 for the control (ipsilateral), n = 12 for Rho activator (ipsilateral); n = 10 for the control (contralateral), n = 11 for Rho activator (contralateral), mean ± s.e.m., one-way ANOVA (no adjustment). **g**, Optogenetic activation of RhoA increased Flipper-TR lifetime during 488-nm illumination, n = 7, paired t-test. *$p < 0.05$, **$p < 0.01$.

Fig. 5. RhoA-dependent regulation of HCN channel gating via OMD expansion in neuropathic pain. **a**, Representative HCN current traces illustrating that RhoA activation decelerates channel activation. Red traces indicate double-exponential fits of the current at -140 mV. Spontaneous action potentials recorded from the same SNI neuron are also shown: untreated neurons (control) exhibited spontaneous firing, whereas neurons treated with the Rho activator did not. **b**-**d**, Summary of the parameters from Boltzmann fit of the G-V relationship for HCN channel activation before and after the RhoA activator treatment of SNI small DRG neurons: activation time constant (τ_1) in panel b, $V_{1/2}$ in panel c and slope factor (V_s) in panel d, n = 10 patches for the control and n = 6 patches for the Rho activator condition, *$p < 0.05$, **$p < 0.01$, two-sided t-test. **e**-**g**, Summary of the parameters from Boltzmann fit of the G-V relationship of HCN channel activation before and after the RhoA inhibitor treatment of naïve small DRG neurons: activation time constant (τ_1) in panel e, $V_{1/2}$ in panel f and slope factor (V_s) in panel g, n = 9 patches for the control, n = 6 for τ_1 of HCN activation under the RhoA activator condition, and n = 9 (control) and 10 (Rho inhibitor) for $V_{1/2}$ and V_s of the G-V curve fits for HCN activation, *$p < 0.05$, **$p < 0.01$, two-sided t-test. **h**-**i**, Summary schematic illustrating the mechanisms by which RhoA activity attenuates neuronal hyperexcitability through increased membrane lateral tension, coalescence of OMDs, and reduced HCN channel activity. OMDs remain dispersed under low tension (pain state, h) and coalesce into larger domains when lateral tension increases due to RhoA activation (i).

Fig. 1

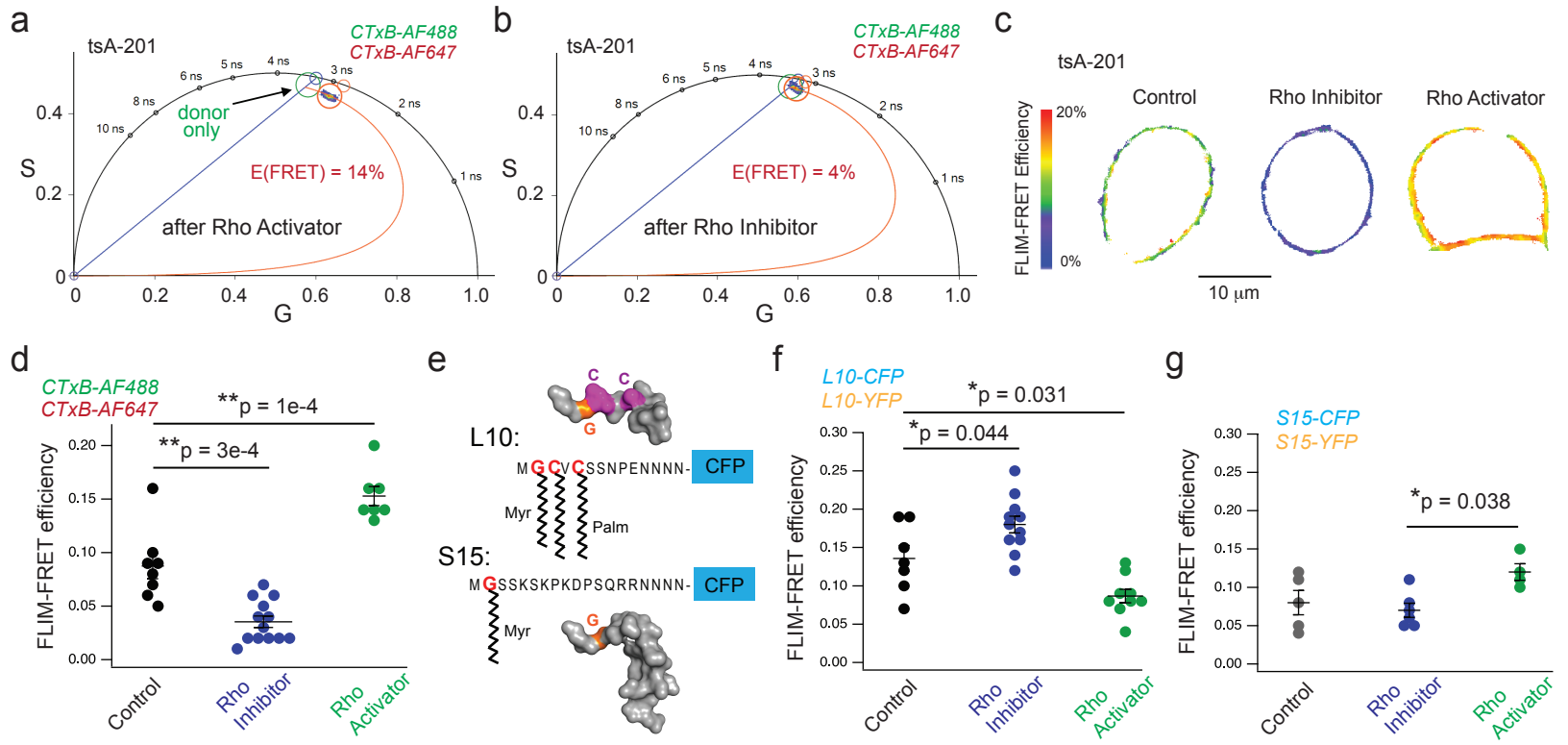
a
tsA-201
CTxB-AF488
CTxB-AF647
donor only
E(FRET) = 14%
after Rho Activator
S
G
b
tsA-201
CTxB-AF488
CTxB-AF647
E(FRET) = 4%
after Rho Inhibitor
c
tsA-201
Control
Rho Inhibitor
Rho Activator
FLIM-FRET Efficiency
20%
0%
10 µm
d
CTxB-AF488
CTxB-AF647
**p = 1e-4
**p = 3e-4
FLIM-FRET efficiency
Control
Rho Inhibitor
Rho Activator
e
L10:
MGCVCSSNPENNNN-
CFP
Myr
Palm
S15:
MGSSKSKPKDPSQRRNNNN-
CFP
Myr
f
L10-CFP
L10-YFP
*p = 0.031
*p = 0.044
FLIM-FRET efficiency
Control
Rho Inhibitor
Rho Activator
g
S15-CFP
S15-YFP
*p = 0.038
FLIM-FRET efficiency
Control
Rho Inhibitor
Rho Activator

Fig. 2

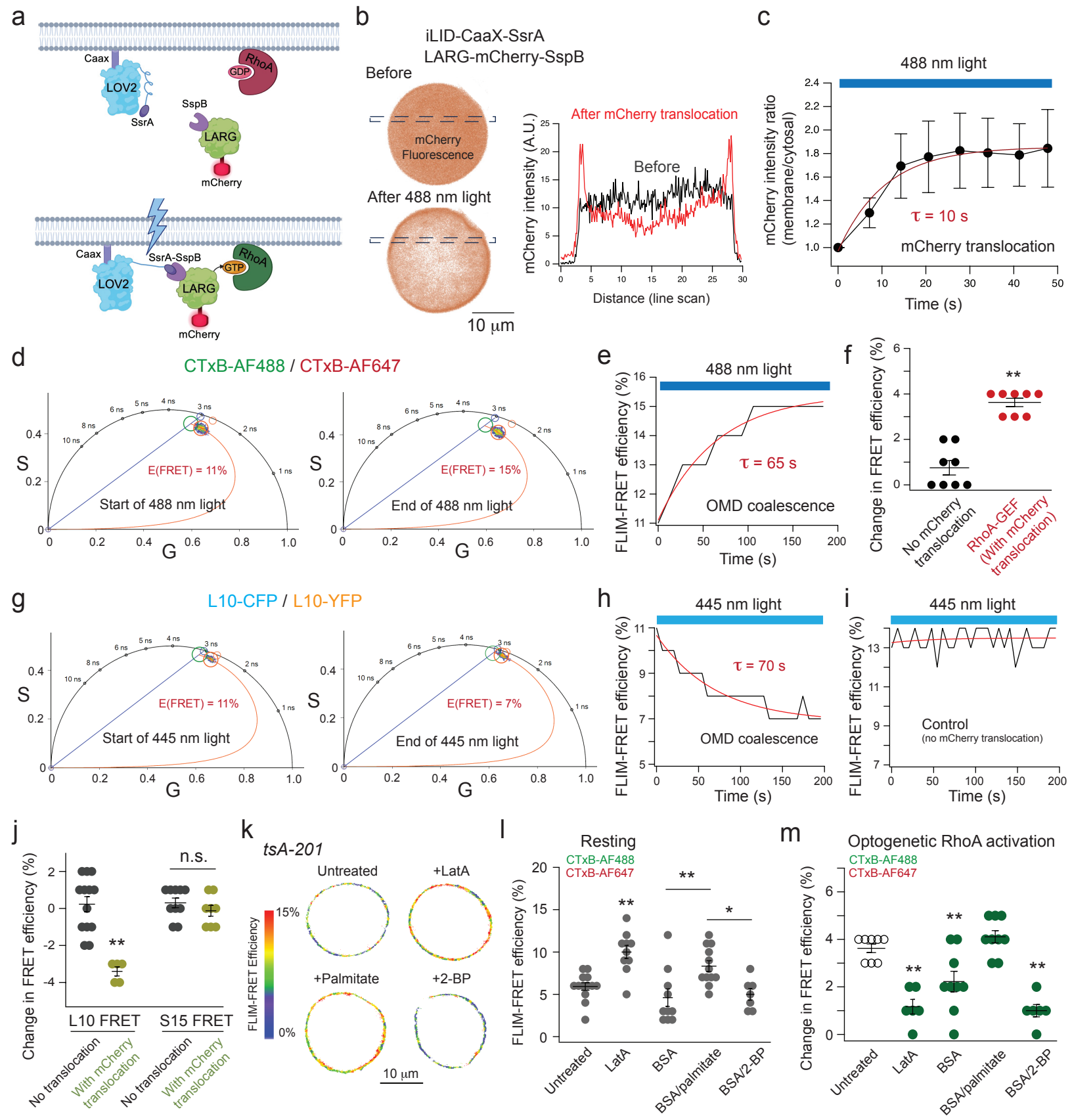
a
Caax
LOV2
SsrA
RhoA
GDP
SspB
LARG
mCherry
SsrA-SspB
GTP
b
iLID-CaaX-SsrA
LARG-mCherry-SspB
Before
mCherry Fluorescence
After 488 nm light
10 µm
After mCherry translocation
Before
mCherry intensity (A.U.)
Distance (line scan)
c
488 nm light
mCherry intensity ratio (membrane/cytosol)
τ = 10 s
mCherry translocation
Time (s)
d
CTxB-AF488 / CTxB-AF647
E(FRET) = 11%
Start of 488 nm light
E(FRET) = 15%
End of 488 nm light
S
G
e
488 nm light
FLIM-FRET efficiency (%)
τ = 65 s
OMD coalescence
Time (s)
f
Change in FRET efficiency (%)
No mCherry translocation
RhoA-GEF (With mCherry translocation)
g
L10-CFP / L10-YFP
E(FRET) = 11%
Start of 445 nm light
E(FRET) = 7%
End of 445 nm light
h
445 nm light
τ = 70 s
OMD coalescence
i
445 nm light
Control
(no mCherry translocation)
j
n.s.
L10 FRET
S15 FRET
No translocation
With mCherry translocation
k
tsA-201
Untreated
+LatA
+Palmitate
+2-BP
FLIM-FRET Efficiency
15%
0%
10 µm
l
Resting
CTxB-AF488
CTxB-AF647
Untreated
LatA
BSA
BSA/palmitate
BSA/2-BP
m
Optogenetic RhoA activation
CTxB-AF488
CTxB-AF647
Untreated
LatA
BSA
BSA/palmitate
BSA/2-BP

Fig. 3

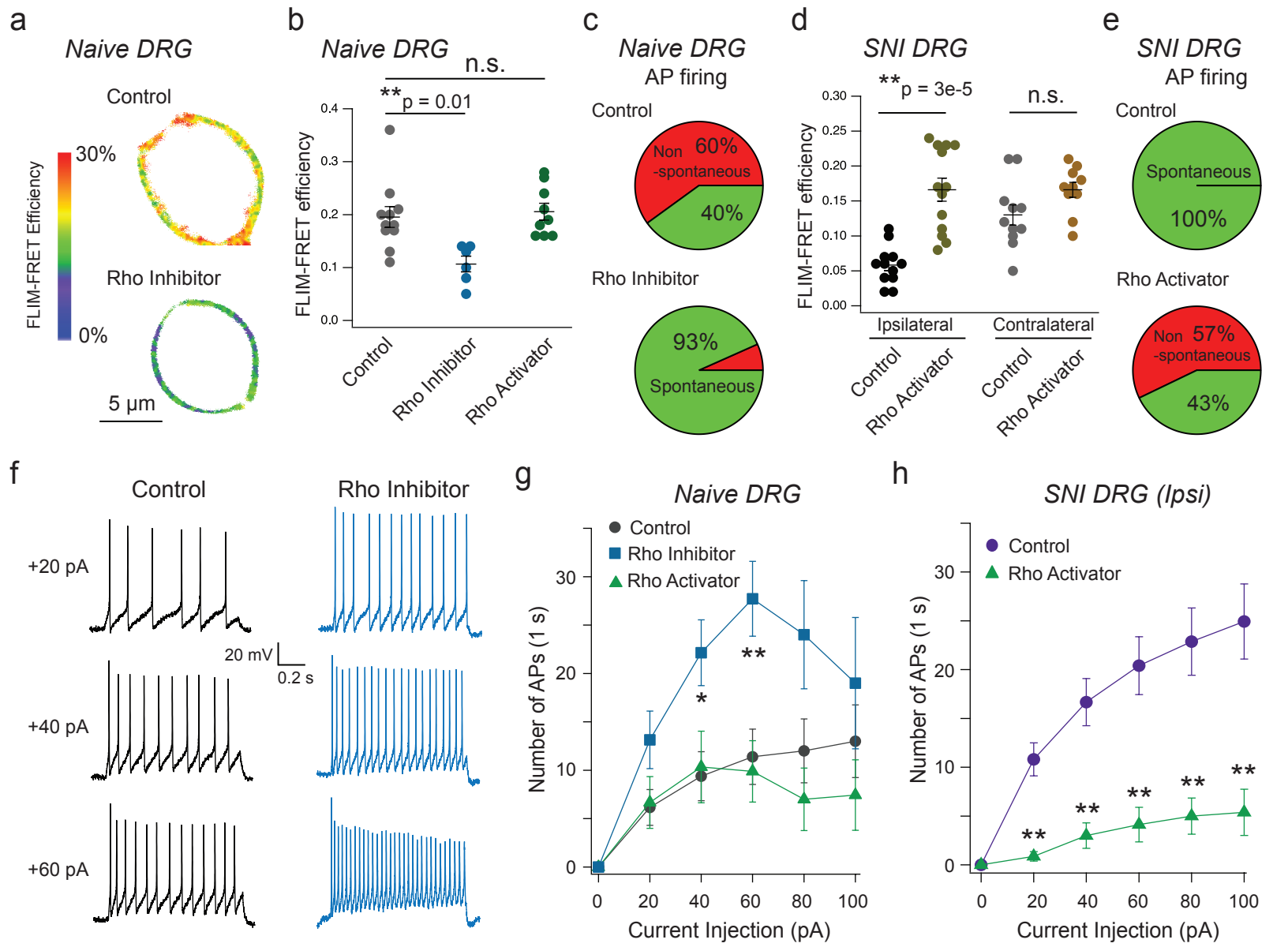
a
Naive DRG
Control
30%
0%
FLIM-FRET Efficiency
Rho Inhibitor
5 µm
b
Naive DRG
n.s.
**p = 0.01
FLIM-FRET efficiency
0.4
0.3
0.2
0.1
0.0
Control
Rho Inhibitor
Rho Activator
c
Naive DRG
AP firing
Control
Non -spontaneous
60%
40%
Rho Inhibitor
93%
Spontaneous
d
SNI DRG
**p = 3e-5
n.s.
FLIM-FRET efficiency
0.30
0.25
0.20
0.15
0.10
0.05
0.00
Ipsilateral
Contralateral
Control
Rho Activator
Control
Rho Activator
e
SNI DRG
AP firing
Control
Spontaneous
100%
Rho Activator
Non -spontaneous
57%
43%
f
Control
Rho Inhibitor
+20 pA
+40 pA
+60 pA
20 mV
0.2 s
g
Naive DRG
Control
Rho Inhibitor
Rho Activator
Number of APs (1 s)
30
20
10
0
*
**
0
20
40
60
80
100
Current Injection (pA)
h
SNI DRG (Ipsi)
Control
Rho Activator
Number of APs (1 s)
30
20
10
0
**
**
**
**
**
0
20
40
60
80
100
Current Injection (pA)

Fig. 4

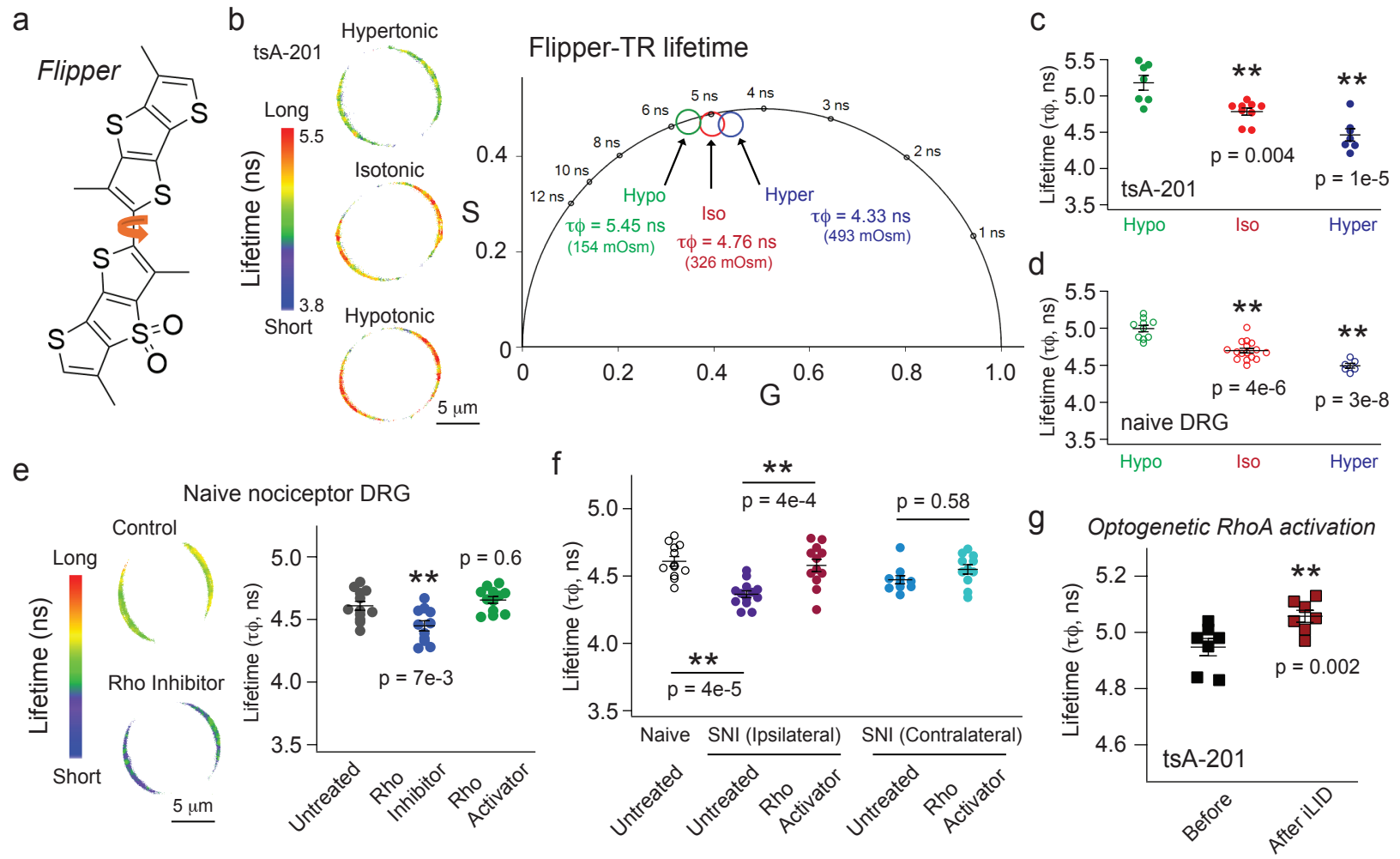
a
Flipper
b
tsA-201
Hypertonic
Isotonic
Hypotonic
Long
Short
Lifetime (ns)
5.5
3.8
5 µm
Flipper-TR lifetime
S
G
Hypo
Iso
Hyper
τϕ = 5.45 ns
(154 mOsm)
τϕ = 4.76 ns
(326 mOsm)
τϕ = 4.33 ns
(493 mOsm)
c
tsA-201
Lifetime (τϕ, ns)
p = 0.004
p = 1e-5
d
naive DRG
p = 4e-6
p = 3e-8
e
Naive nociceptor DRG
Control
Rho Inhibitor
p = 7e-3
p = 0.6
Untreated
Rho Inhibitor
Rho Activator
f
p = 4e-4
p = 0.58
p = 4e-5
Naive
SNI (Ipsilateral)
SNI (Contralateral)
g
Optogenetic RhoA activation
p = 0.002
Before
After iLID

Fig. 5

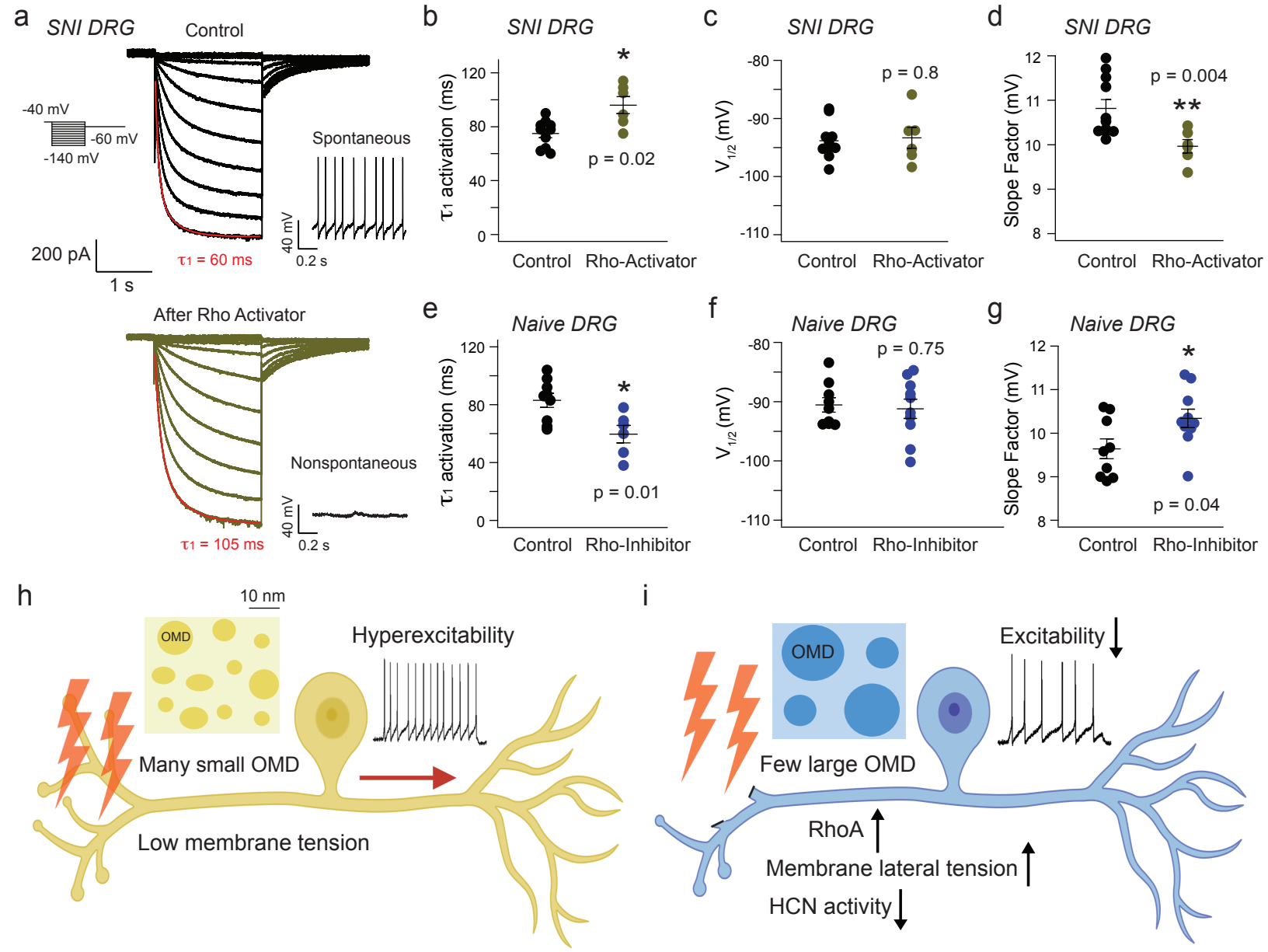
a
SNI DRG
Control
-40 mV
-60 mV
-140 mV
Spontaneous
200 pA
1 s
τ1 = 60 ms
40 mV
0.2 s
After Rho Activator
Nonspontaneous
τ1 = 105 ms
b
SNI DRG
τ1 activation (ms)
p = 0.02
Control
Rho-Activator
c
SNI DRG
V1/2 (mV)
p = 0.8
d
SNI DRG
Slope Factor (mV)
p = 0.004
e
Naive DRG
p = 0.01
Rho-Inhibitor
f
Naive DRG
p = 0.75
g
Naive DRG
p = 0.04
h
10 nm
OMD
Hyperexcitability
Many small OMD
Low membrane tension
i
OMD
Excitability
Few large OMD
RhoA
Membrane lateral tension
HCN activity